



Article

A Combined Paddy Field Inter-Row Weeding Wheel Based on Display Dynamics Simulation Increasing Weed Mortality

Jinwu Wang ¹, Zhe Liu ¹, Mao Yang ¹, Wenqi Zhou ¹, Han Tang ¹, Long Qi ², Qi Wang ^{1,*} and Yi-Jia Wang ^{3,*}

¹ College of Engineer, Northeast Agricultural University, Harbin 150030, China; jinwuw@neau.edu.cn (J.W.); s210701019@neau.edu.cn (Z.L.); s230702073@neau.edu.cn (M.Y.); zwq@neau.edu.cn (W.Z.); tanghan@neau.edu.cn (H.T.)

² College of Engineer, South China Agricultural University, Guangzhou 510642, China; qilong@scau.edu.cn

³ School of Water Conservancy & Civil Engineering, Northeast Agricultural University, Harbin 150030, China

* Correspondence: wangqi@neau.edu.cn (Q.W.); yijia@connect.hku.hk (Y.-J.W.)

Abstract: Weeds compete with rice for sunlight and nutrients and are prone to harboring pathogens, leading to reduced rice yields. Addressing the issues of low weeding efficiency and weed mortality rates in existing inter-row weeding devices, the study proposes the design of a combination paddy field inter-row weeding wheel. The device's operation process is theoretically analyzed based on the weed control requirements in the northeastern region of China, leading to the determination of specific structural parameters. This research conducted experiments on the mechanical properties of weed cutting to obtain geometric parameters for paddy field weeds. It was found that the range for the cutting gap of the dynamic-fixed blade is between 0.6 mm to 1.4 mm and the cutting angle is between 5° to 15°, resulting in the lowest peak cutting force for weeds. Using LS-DYNA R12.0.0 dynamic simulation software, a fluid-structure interaction (FSI) model of the weeding wheel-water-soil system was established. By employing the central composite experimental design principle and considering the soil stir rate and coupling stress as indicators, the optimal structural parameter combination for the device is obtained: a dynamic-fixed blade cutting gap of 1.4 mm, a cutting angle of 10.95°, and a dynamic blade install angle of -3.44°. Field experiments demonstrated that the device achieved an average weeding rate of 89.7% and an average seedling damage rate of 1.9%, indicating excellent performance. This study contributes to improving weed mortality rates and provides valuable guidance for inter-row mechanical weeding technology.

Keywords: paddy field; mechanical weeding; combination of dynamic-fixed blade; weed cutting mechanical properties; finite element method



Citation: Wang, J.; Liu, Z.; Yang, M.; Zhou, W.; Tang, H.; Qi, L.; Wang, Q.; Wang, Y.-J. A Combined Paddy Field Inter-Row Weeding Wheel Based on Display Dynamics Simulation Increasing Weed Mortality. *Agriculture* **2024**, *14*, 444. <https://doi.org/10.3390/agriculture14030444>

Academic Editor: Valentin Vlăduț

Received: 30 January 2024

Revised: 28 February 2024

Accepted: 6 March 2024

Published: 8 March 2024



Copyright: © 2024 by the authors. Licensee MDPI, Basel, Switzerland. This article is an open access article distributed under the terms and conditions of the Creative Commons Attribution (CC BY) license (<https://creativecommons.org/licenses/by/4.0/>).

1. Introduction

Rice is a staple food for over half of the world's population and contains essential vitamins and minerals important for human health [1,2]. The global demand for rice has been steadily increasing. However, weeds in paddy fields compete with crops for nutrients, growth space, and sunlight, and they can also spread diseases and pests, significantly reducing rice yields [3,4]. In recent years, the increasing resistance of weeds to herbicides has led to higher herbicide residues, posing serious health risks to animals and humans through the food chain [5–7]. Mechanical weeding has gained attention due to its advantages, such as its lack of chemical contamination, rapid effectiveness, improvement of the soil's physical properties, and enhanced soil aeration [8–10]. Efficient mechanical weeding techniques and equipment are of paramount importance for high-quality rice production [11].

In European and American countries, rice cultivation is typically done via aerial seeding, which makes mechanical weeding operations challenging. Research in these regions has primarily focused on the efficient use of herbicides [12–15], but the excellent weeding equipment developed for dryland farming is worth considering [16,17]. In China, rice is often transplanted mechanically, allowing for the orderly growth of seedlings in the field,

which is conducive to the sustainable development of inter-row weeding machinery [18]. Machines like the 3GY-1920 wide-width paddy inter-row weeder can cover the working width of three transplanter passes in a single operation, reducing the seedling damage caused by frequent turns [19]. Electric double-row deep fertilizer and stepwise weeding machines can simultaneously perform rice tillering deep fertilization and inter-row weeding operations [20]. Wang et al. [21] designed a remotely controlled inter-row weeding machine capable of removing two rows of weeds in one pass, achieving a weeding rate of no less than 77.9%. Zhang et al. [22], through simulation software, optimized the angle of the rake teeth based on the resistance it encountered and the velocity of the soil particles, resulting in a weeding rate of 88.2%. However, the inter-row weeding wheels used in these machines are passively rotating or electrically driven and rely on the weeding wheel tines to bury or pull out weeds. They do not have a mechanism to cut and shred the weeds. The mortality rate of weeds after being pulled out is only 47–61%, and for those buried, the mortality rate is only 1–17% [23]. Therefore, it is meaningful to use a weeding device to cut and break the weeds, but there has been no related research reported so far.

Research on stem cutting characteristics is essential for the development of efficient and low-power cutting. Numerous studies on this topic have been conducted. Soleimani et al. [24] investigated the mechanical cutting characteristics and energy consumption of sesame stems under different cutting speeds, moisture levels, and cutting positions. Chattopadhyay et al. [25] found that the energy consumption was minimal when the blade angle was 20° during cutting grazing. Allameh et al. [26] conducted cutting tests on different rice varieties and found that the rice variety and cutting speed had a significant effect on the specific cutting energy, while the cutting angle and blade skew angle had little effect. Song et al. [27] studied the effect of different cutting parameters on the cutting force and cutting power consumption of flax, finding that the ultimate shear stress decreased by 93.51% when the blade angle increased from 0° to 45°. Aydin et al. [28] conducted shear tests on cotton seedlings using a universal testing machine and found that the maximum shear force near the top of the cotton seedling was 73 N, while the maximum shear force away from the top was 121 N. Due to the presence of weed seeds in the topsoil of paddy fields over several seasons, and the varying depths at which the seeds are buried in the soil, weeds germinate at different times, affecting the growth of rice at different growth stages and to different extents [29,30]. Therefore, it is crucial to study the effect of weeding wheel tine parameters on the cutting characteristics of paddy weeds during different weeding periods. This is of great significance for improving weed shredding performance and weeding efficiency but has not been reported in previous studies.

In the research on the interaction between agricultural machinery and soil, discrete element software is often used for simulation tests. These studies mainly focus on dryland soil [31–33]. However, paddy fields consist of both water and soil layers, creating a more complex working environment. Discrete element simulation software is no longer suitable for studying the interaction between agricultural machinery and paddy fields. Therefore, scholars have increasingly turned to finite element simulation software, such as LS-DYNA, to create simulated paddy field environments. Wang et al. [34] used LS-DYNA simulation software to investigate the soil disturbance caused by their designed inter-row weeding device. Zhou et al. [35], based on theoretical analysis, used LS-DYNA simulation technology to optimize the structural parameters of their designed jet-type paddy field weeding device. Fragassa et al. [36], using a combination of smoothed particle hydrodynamics and finite element methods, analyzed the effect of air convection on fluid–solid coupling results. Rokhy et al. [37] conducted fluid–solid coupling simulations of the explosion process of mixed gases using LS-DYNA®. Therefore, in this study, LS-DYNA simulation software was also used to optimize the structural parameters of the weeding wheel.

In summary, the process of this research involves: (1) a theoretical analysis and calculation to determine the main structural parameters of the weeding wheel; (2) controlled experiments using a universal testing machine to investigate the effect of the cutting gap and cutting angle of the dynamic–fixed blade on the peak cutting force of paddy

weeds; (3) the optimization of key structural parameters of the weeding wheel through an LS-DYNA explicit dynamics simulation and a three-factor, five-level central composite experiment design, using the soil stir rate and coupling stress as indicators; and (4) field experiments to validate the performance of the device. This study provides new insights into mechanical weeding technology in paddy fields and contributes to the green and sustainable development of agriculture.

2. Materials and Methods

2.1. Overall Structure and Working Principle of the Combination Rice Field Inter-Row Weeding Wheel

The combination rice field inter-row weeding wheel's design and operation are presented in Figure 1. The mounting bracket (4) is securely welded to the fixed shaft (11), forming the primary structure for the two symmetrically arranged weeding rollers. Each weeding roller consists of a dynamic blade assembly and a stationary blade assembly. The dynamic blade (5) is welded in the circumferential direction of the blade ring (13) and the outer dynamic blade disc (8). After welding, this assembly is bolted to the dynamic blade disc (8) near the mounting bracket (4), creating the dynamic blade assembly. Bearings (14) and circlips (15) are utilized on both sides of the dynamic blade assembly for precise positioning. The stationary blade assembly is formed by welding the pre-fixed blade (7), rear-fixed blade (12), and bushing (10) between two triangular fixed-blade holders (6). The fixed-blade assembly is firmly secured in place by a split pin (9) passing through the bushing (10) and a through-hole on the fixed shaft (11). To connect the mounting bracket (4) and the brace (1), hinged bolts (3) are employed, and imitation springs (2) are attached at both ends, linking the mounting bracket (4) and the brace (1).

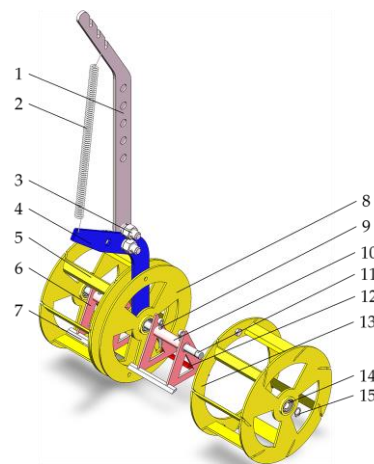


Figure 1. Schematic structure of combined paddy field inter-row weeding wheel. 1. Brace; 2. Imitation spring; 3. Hinged bolt; 4. Mounting bracket; 5. Dynamic blade; 6. Fixed-blade holder; 7. Pre-fixed blade; 8. Dynamic blade disc; 9. Split pin; 10. Bushing; 11. Fixed shaft; 12. Rear-fixed blade; 13. Blade ring; 14. Bearing; 15. Circlip.

The weeding wheel operates passively, driven by the traction provided by the walking device. Prior to initiating the operation, the weeding wheel should be positioned within the rows on either side of the rice seedlings. The depth of the soil penetration can be adjusted by connecting the weeding wheel to the walking device through various mounting holes on the brace (1). To adapt to different field conditions, the attachment level of the imitation spring (2) can be modified, thereby reducing the effect of uneven terrain on the working depth. During operation, weeds are drawn into the interior of the weeding wheel as it advances. The pre-fixed blade (7) closely conforms to the soil surface, providing support and facilitating the cutting of entrapped weeds within the weeding wheel. The effective cutting of weed stems is achieved through the dynamic–fixed cutting relationship

established between the dynamic blade (5) and the pre-fixed blade (7). The front blade edge of the rear-fixed blade (12), located beneath the slurry, effectively removes any weeds that have not been entrapped within the weeding wheel. As the dynamic blade (5) leaves the soil, a dynamic–fixed cutting relationship forms between the rear blade edge of the rear-fixed blade (12) and the dynamic blade (5), aiding in the detachment of soil from the dynamic blade (5). While ensuring the device’s operational width, the weeding wheel employs a brace suspension structure, mitigating the traditional issue of mounting brackets potentially scraping or damaging rice seedlings at both ends.

2.2. Device Design

2.2.1. Rice Planting and Weed Control Agricultural Requirements in Northeastern China

Based on information derived from references [38,39], when rice seedlings are mechanically transplanted, the standard row spacing is 300 mm, with a plant spacing of 150 mm, and the paddy fields are typically submerged in water to a depth ranging from 30 to 50 mm. Following the transplantation of rice seedlings, it is crucial to ensure that they are uniformly distributed, arranged neatly, and aligned in straight rows. This alignment is vital to facilitate the operation of weed control devices. The most opportune period for inter-row weeding generally falls within the 10–20 d window after transplantation. During weeding activities, the depth of rice roots typically extends to 80–100 mm. On either side of the root system in the inter-row direction, a 50 mm-wide area, referred to as the rice inter-row single-sided seedling avoidance area, is present. Furthermore, it is essential to note that the height of weeds should not exceed 240 mm, with weed root systems typically penetrating to depths ranging from 20 to 50 mm. To ensure effective weed control, the inter-row weeding rate must consistently surpass the 75% threshold. An illustration of rice planting and weed control agronomic requirements as shown in Figure 2.

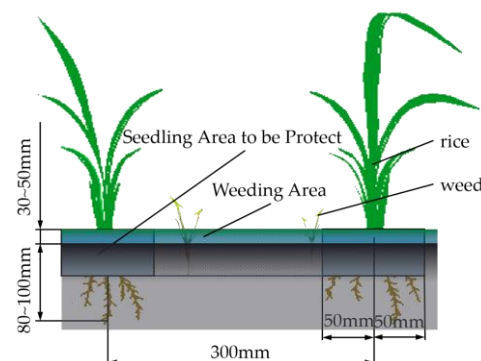


Figure 2. Illustration of rice planting and weed control agronomic requirements.

2.2.2. Designing Device Structural and Operating Parameters

As illustrated in Figure 3a, the theoretical operational width of this device comprises the theoretical operational widths of the two weeding rollers on both sides and the width of the central gap. To ensure the protection of rice seedlings from any potential damage, it is imperative that the working width of each component of the weeding wheel complies with Equations (1) and (2).

$$B = 2B_1 + B_2 \quad (1)$$

$$2r_1 + B \leq D \quad (2)$$

where B is the theoretical working width of the combined paddy field inter-row weeding wheel (mm); B_1 is the theoretical working width of a single weeding roller (mm); B_2 is the width of the gap between two weeding rollers (mm); r_1 is the width of the single-side seedling avoidance area in the rice inter-row (mm); D is the rice planting row spacing (mm).

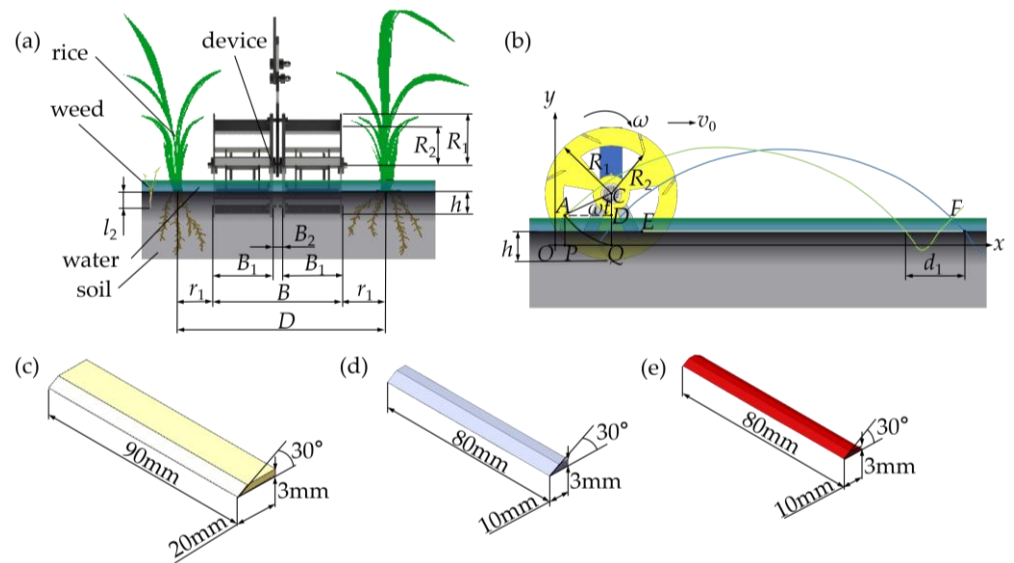


Figure 3. Schematic diagram of the device working parameters and structural parameters. (a) Paddy field inter-row weed control environment; (b) Weed control wheel movement trajectory; (c) Dynamic blade dimensions; (d) Pre-fixed blade dimensions; (e) Rear-fixed blade dimensions.

To avoid damage to the rice seedling root system beneath the mud surface from the weeding wheel and ensure that the rotating and fixed blades cut through the weed roots, the depth to which the weeding wheel is inserted into the soil should satisfy Equations (3) and (4).

$$h \leq 80 \tag{3}$$

$$0 \leq h \leq l_1 \tag{4}$$

where h is the depth of the weeding wheel’s penetration into the soil (mm); l_1 is the average depth of the weed roots in the paddy field (mm).

Therefore, B is designed to be 200 mm, B_1 is 90 mm, and B_2 is 20 mm. Subsequently, l_1 was measured to be 51 mm, thereby h was designed to be 40 mm.

As shown in Figure 3b, the x -axis represents the forward direction, and the device undergoes passive rotation while moving forward (in the clockwise direction, as shown in the figure). The motion of the dynamic blade is a composite motion consisting of its rotational motion around the weeding wheel’s fixed-shaft and its linear motion as the device moves forward. R_1 is the radius of the weeding wheel’s dynamic blade disc, and R_2 is the radius of the circle where the dynamic blade edge is located. Taking any point on the dynamic blade edge as the subject of study and assuming that it starts at the origin O at the initial moment, the velocity is v_0 , in an ideal scenario, the weeding wheel’s motion is pure rolling. After time t , it rotates to the position represented by point A . The angle of rotation is ωt . Line EF represents the location of the soil surface, which is also the trajectory of the pre-fixed blade edge. The two cycloids in the diagram represent the trajectories of adjacent dynamic blade edges. By applying trigonometric relationships, the motion equations for any point on the dynamic blade edge can be derived as Equations (5) and (6).

$$OP = OQ - PQ = R_2\omega t - R_2 \sin \omega t \tag{5}$$

$$QD = CQ - CD = R_2 - R_2 \cos \omega t \tag{6}$$

where OP is the distance moved by the dynamic blade edge in the x -direction (mm); QD is the distance moved by the dynamic blade edge in the y -direction (mm); ω is the angular velocity of dynamic blade edges (rad/s); t is time (s).

To prevent the weeding wheel from getting entangled with the weeds, the device must meet the structural requirements specified in Equations (7) and (8).

$$R_1 > R_2 \quad (7)$$

$$2\pi R_2 \geq l_2 \quad (8)$$

where R_1 is the radius of the dynamic blade head (mm); R_2 is the radius of the circle where the dynamic blade edge is located (mm); l_2 is the height of weeds in the paddy field (mm).

During the weeding wheel's operation, the pre-fixed blade moves horizontally forward, causing the weeds to bend under the support of the pre-fixed blade. To ensure that the bent weeds are effectively rolled into the weeding wheel for cutting, it is necessary to design a reasonable arrangement of the number of dynamic blades on a single weeding roller's head. If there are too many dynamic blades, the bent weeds may not be rolled into the weeding wheel effectively during its rotation, resulting in inadequate weed shredding. Conversely, if there are too few dynamic blades, the cutting performance of the weeding wheel may be weakened due to larger soil-cutting spacing. Therefore, the number of dynamic blades on a single weeding roller's head should satisfy Equation (9).

$$Z < \frac{2\pi R_2}{l_3} \quad (9)$$

where Z is the number of dynamic blades on the dynamic blade disc; l_3 is the average height of weeds after bending in the paddy field (mm).

At this point, the soil-cutting spacing between two adjacent dynamic blades d_1 can be determined using Equation (10).

$$d_1 = \frac{2\pi R_2}{Z} \quad (10)$$

where d_1 is the distance between adjacent dynamic blade cutting sections (mm).

The weeding period occurs 10–20 d after transplanting, with $l_2 \leq 240$ mm [39], and l_3 is set at 60 mm. Based on the above data, R_1 is determined to be 90 mm, R_2 is 70 mm, and it is determined that $Z < 7.33$. Taking Z to be 7, d_1 is obtained as 63 mm.

For the design of the dynamic blade, considering both the cutting and burying effects, a length of 90 mm, thickness of 3 mm, and a blade angle of 30° are chosen. To ensure that the dynamic blade can cut the weed and bury it effectively, a width of 20 mm is set. The relevant dimensions are shown in Figure 3c.

The blade edge of the pre-fixed blade does not penetrate the soil but matches the surface of the mud layer. The installation position of the rear-fixed blade edge is 5 mm below the mud layer. Both fixed blade types have a blade angle of 30° . To reduce the resistance generated by the fixed blades during operation, both types of fixed blades have a width of 10 mm. The dimensions of the pre-fixed blade are shown in Figure 3d, and the dimensions of the rear-fixed blade are shown in Figure 3e.

2.2.3. Pending Structural Parameters

In this study, the definitions of the dynamic–static blade cutting gap and cutting angle are as follows: when the pre-fixed blade of the weeding wheel is aligned with the edge of the dynamic blade on the same vertical plane, the distance between the long edges of the two blades is defined as the dynamic–static blade cutting gap d , and the angle between the long edges of the two blades is defined as the dynamic–static blade cutting angle θ , as shown in Figure 4a. The schematic diagram of the dynamic blade install angle α is shown in Figure 4b.

The dynamic–static blade cutting gap will have an effect on the cutting force. Since the blades act on the weed stems at an angle, the dynamic–static blade cutting angle will also affect the cutting force. The theoretical analysis of the process of the dynamic–static blade cutting weed stems is shown in Figure 4c. This study considers a weed root system with a length of a_1 as the research object. Since the weed root system is fixed in the soil, it is

treated as a simply supported beam model. An imaginary cross-section I-I is used to divide this section of the root system into two parts, with lengths a_2 and a_3 .

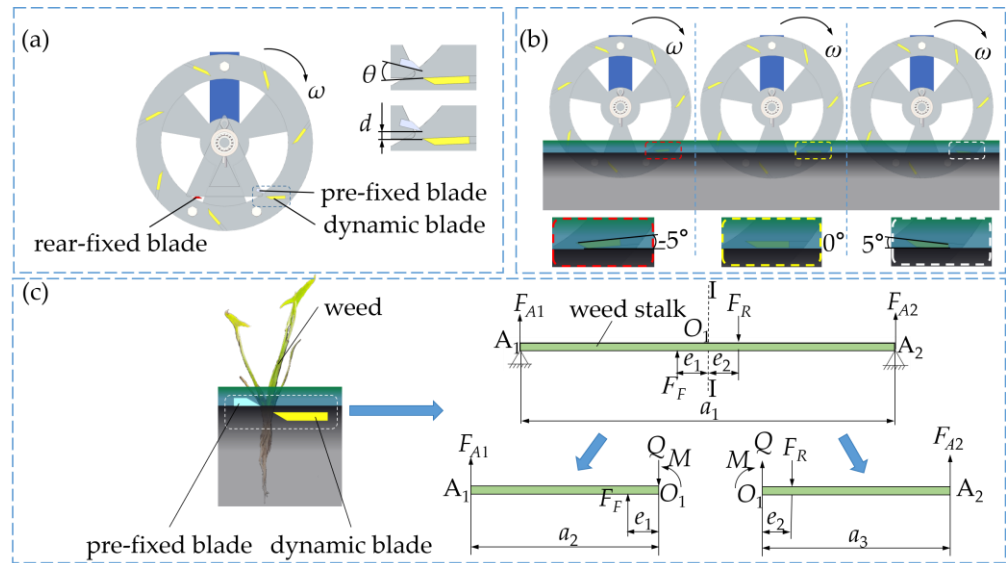


Figure 4. Undetermined structural parameters of the weed control wheel and theoretical analysis of the weed cutting process. (a) Gap and cutting angle of the dynamic–static blade; (b) Dynamic blade install angle; (c) Theoretical analysis of weed cutting by the dynamic–static blade.

Since the weed stems are in equilibrium, all of their parts are also in equilibrium. Based on the equilibrium conditions, equilibrium equations are established as shown in Equations (11) and (12). By solving them simultaneously, the expression for the cutting force F_R of the dynamic blade to the distance e_2 from the dynamic blade edge to cross-section I-I is obtained as shown in Equation (13).

$$\begin{cases} \sum F_y = 0 \\ F_{A1} + F_F - Q = 0 \\ F_{A2} + Q - F_R = 0 \end{cases} \quad (11)$$

$$\begin{cases} \sum M_{O1} = 0 \\ M - F_{A1} \cdot a_2 - F_F \cdot e_1 = 0 \\ F_{A2} \cdot a_3 - F_R \cdot e_2 - M = 0 \end{cases} \quad (12)$$

$$F_R = \frac{M + Q \cdot a_3}{a_3 - e_2} \quad (13)$$

where F_{A1} is the vertical support reaction force on the left end of the weed (N); F_{A2} is the vertical support reaction force on the right end of the weed (N); F_F is the pressure of the fixed blades on the weed roots (N); F_R is the pressure of the dynamic blades on the weed roots (N); Q is the resultant force of weed internal forces tangent to cross-section I-I (N); M is the resultant force moment of weed internal forces perpendicular to cross-section I-I (N·m); a_1 is the research’s weed root length (m); a_2 is the weed root length on the left side of cross-section I-I (m); a_3 is the weed root length on the right side of cross-section I-I (m); e_1 is the distance from the fixed blade edge to cross-section I-I (m); e_2 is the distance from the dynamic blade edge to cross-section I-I (m).

Theoretically, the resultant force Q and moment M of the internal forces that intersect the same cross-section of the same weed species are constant. Therefore, when the fixed blade edge remains flush with the soil surface, e_1 remains constant. An increase in the dynamic–static blade cutting gap d leads to an increase in e_2 , resulting in an increased pressure F_R applied by the dynamic blade on the weed root system.

In the actual operational process, the dynamic blade install angle provides the driving force for the weeding wheel's rotation. Therefore, based on the existing entry angle of teeth for row weeding wheels [38], the range of values for α in this device is selected as -5° to 5° .

Since the effect of these three structural parameters on the weed cutting force is difficult to calculate through theoretical analysis, specific values will be determined through subsequent experiments on the mechanical properties of weed cutting and simulation experiments.

2.3. Paddy Field Weed Cutting Mechanical Properties Experiment

2.3.1. Experimental Materials and Equipment

Barnyard grass and arrowhead are common weeds in paddy fields [40,41]. In this study, weed leaf age was used as a classification criterion for their growth stage and degree of growth [42]. Common paddy field weeds were collected in June 2022 from a paddy field located in Chenggaozi Town, Xiangfang District, Harbin City, Heilongjiang Province (126.903° E, 45.699° N) as experimental materials: barnyard grass with a leaf age between 3 to 4.5 (BA-345), barnyard grass with a leaf age between 5 to 8 (BA-58), arrowhead with a leaf age between 3 to 5 (AR-35), and arrowhead with a leaf age between 5.5 to 8 (AR-558). At that time, the rice in this field had been mechanically transplanted for 16 d, and no herbicides had been applied. To minimize the effect of changes in weed moisture content on the test results, the collected weeds were placed in sealed bags and transported to the laboratory of the College of Engineering at Northeast Agricultural University for timely testing [43].

The experimental materials and required equipment are shown in Figure 5. The equipment includes: dynamic blades and fixed blades (made of Q235 steel, 3 mm thick, with a blade angle of 30°); A 3D-printed fixture was fabricated to secure the blades and weeds; A YHS-216W-500N universal testing machine (Shanghai Yiheng Instrument Technology Co., Ltd., Shanghai, China) and a U10A S-type pressure sensor (Shanghai Jiuzhi Sensor Co., Ltd., Shanghai, China) were used; In addition, vernier calipers (accuracy 0.02 mm) and a steel ruler (accuracy 0.5 mm) were used to measure the geometric parameters of the paddy field weeds.

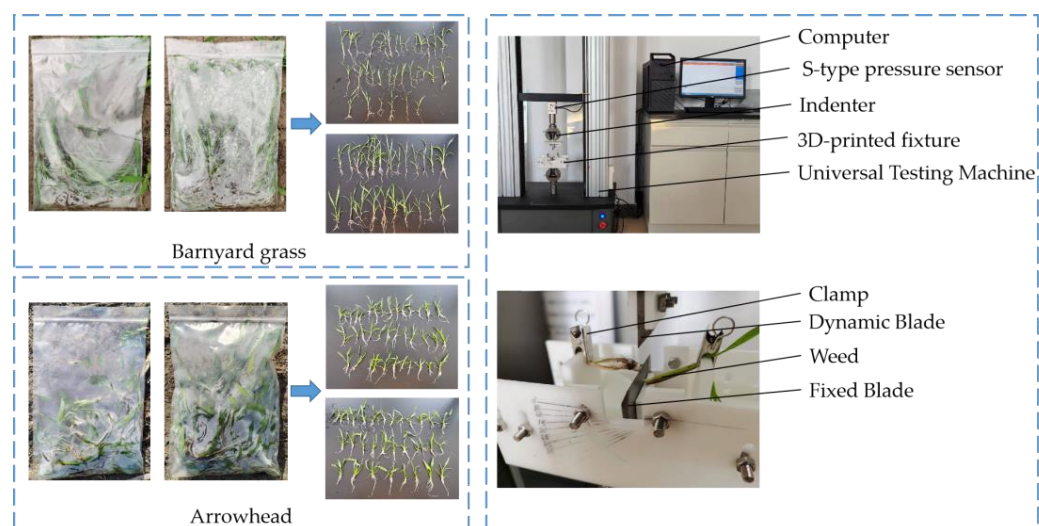


Figure 5. Test materials and instrumentation.

2.3.2. Experimental Method

To obtain the reasonable range of the cutting gap and cutting angle between the dynamic blade and the fixed blade in the simulation tests in Section 2.4, two single-factor tests on the mechanical properties of weed cutting were carried out. The experimental indicators for both single-factor tests were the peak cutting force of the weeds. In the first single-factor experiment, the dynamic—static blade cutting angle was held constant at 15° , while the dynamic—static blade cutting gap was set at 5 levels: 0.2 mm, 0.6 mm, 1 mm, 1.4 mm,

and 1.8 mm. In the second single-factor experiment, the dynamic–static blade cutting gap was kept constant at 1 mm, and the dynamic–static blade cutting angle was varied across 7 levels: 0°, 5°, 10°, 15°, 20°, 25° and 30°. Each level was repeated five times. Initially, a polynomial regression analysis was performed on the experimental results, followed by a one-way ANOVA using SPSS 26 (International Business Machines Corporation, NYC, NY, USA) software, considering a p -value < 0.05 as statistically significant. In order to ensure the validity of the study and reduce the interference of selection bias and confounding factors, we implemented a simple randomized layout. That is, the sequence of tests is determined by a table of random numbers generated by a computer.

Different parts of plant stems produce different cutting forces [44]. Therefore, before the experiment, the stems were marked with a marker pen at a distance h_1 from their base to ensure that the blades cut at the marked location, reducing experimental errors due to different cutting locations. The weed was cut at a controlled rate of 8.3×10^{-3} m/s using an S-type pressure sensor, which recorded the force–time curve and transmitted it to the computer.

2.4. Structural Parameter Optimization Based on LS-DYNA

The structural parameters of the weeding device affect the degree of disturbance to the soil and the resistance it experiences. The soil stir rate reflects the weeding rate of the device, while coupling stress reflects the resistance the device encounters [45]. Since it is difficult to adjust structural parameters in field experiments, a coupled simulation model of the weeding wheel–water–soil was established using LS-DYNA R12.0.0 (Ansys, PIT, Canonsburg, PA, USA) explicit dynamics software to determine the optimal combination of the device’s structural parameters through simulation tests.

2.4.1. Establishment of the Weeding Wheel–Water–Soil Coupled Model

A three-dimensional model of the weeding wheel was created using SolidWorks 2021 (Dassault Systemes, Paris, Ile-de-france region, France) software. To improve simulation efficiency, eliminate irrelevant components, and simplify the weeding device, the model was processed. After completing the model processing, it was imported into the pre-processing software HyperMesh 2019 (Altair Engineering, Troy, MI, USA). The weeding wheel was meshed with a 0.5-unit size, and the output .k file was imported into LS-PrePost 4.3 (Ansys, PIT, Canonsburg, PA, USA) for keyword definition.

The structured arbitrary lagrangian-eulerian (S-ALE) algorithm was used for simulation analysis. The mesh distribution information in three directions was specified using ALE_STRUCTURED_MESH_CONTROL_POINTS and ALE_STRUCTURED_MESH keywords to generate the fluid domain. The dimensions of the water layer model (length \times width \times height) were set to 1000 mm \times 200 mm \times 30 mm, and the dimensions of the soil layer model (length \times width \times height) were set to 1000 mm \times 200 mm \times 120 mm to automatically partition the water–soil mesh. The model is shown in Figure 6a,b.

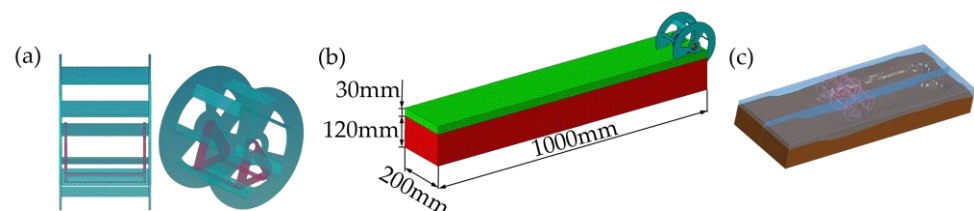


Figure 6. Establishment and simulation process of the fluid–structure coupling model. (a) Finite element model of weed control wheel; (b) Fluid–structure coupling model of weed control wheel–water–soil; (c) Simulation effects.

The simulation materials and parameters in this paper were referenced from previous studies [35,46], as shown in Table 1.

Table 1. Parameter Table of Materials Used in Simulation.

Material	Parameter	Value
Water	Material index	9
	Density (kg/m ³)	1000
	Cutoff pressure (Pa)	−10
	Viscosity coefficient (Pa/s)	8.68×10^8
Soil	Material index	147
	Density (kg/m ³)	1610
	Shear modulus (Pa)	1.9×10^6
	Bulk modulus (Pa)	5.6×10^6
	Cohesion (Pa)	1.55×10^4
	Internal friction angle (°)	15
Weeding Wheel	Moisture content (%)	40
	Material index	20
	Density (kg/m ³)	7850
	Young's modulus (Pa)	2.12×10^{11}
	Poisson's ratio	0.288

The contact area was specified using the DEFINE_BOX keyword to restrict the program to consider contact operations only within that area. The ALE_STRUCTURED_FSI keyword was employed for fluid–structure interaction (FSI) settings, coupling rigid bodies with the Lagrangian algorithm, and coupling them separately with water and soil to achieve dynamic analysis. The EOS_GRUNEISEN keyword was used to set the equation of state for the water. Considering the different motion states between the dynamic–fixed blades, the CONSTRAINED_RIGID_BODIES keyword was used to connect the fixed-blade holder with the fixed blade and the dynamic-blade disc with the dynamic blade. The DEFINE_CURVE keyword was used to set the forward velocity and rotational speed of the weeding wheel, enabling the rotational and translational motion of the dynamic blade and the fixed blade in the same space. The BOUNDARY_PRESCRIBED_MOTION_RIGID keyword was used to apply velocity and displacement boundary conditions to the rigid bodies. The BOUNDARY_SCALE_MESH_FACE keyword was used to fully constrain the bottom layer of the soil, apply non-reflective boundary conditions to the water–soil interface, and impose symmetric boundaries. The LOAD_BODY_Z keyword was used to apply gravity. The HOURGLASS keyword was used for hourglass control on the fluid. After completing these settings, the .k file was imported into LS-DYNA solver for computation, and the generated d3plot file was imported into LS-PrePost for result analysis. The simulation effects are shown in Figure 6c.

2.4.2. Experimental Method

To determine the optimal combination of structural parameters for the dynamic–static blade cutting gap, the dynamic–static blade cutting angle, and the dynamic blade install angle that makes the performance of the weeding device optimal, a three-factor, five-level simulation experiment was conducted using the central composite design principle in Design-Expert 8.0.6 software. Building on the single-factor experiments described earlier, and in conjunction with the theoretical analysis provided, the experimental factors considered were the parameters d , θ , and α of the device. The evaluation criteria were the soil stir rate y_1 and coupling stress y_2 . The response surface method was used to analyze the experiment results, and the corresponding mathematical model was established. The F-test was performed at a $p = 0.05$ level. The levels of experimental factors were encoded as shown in Table 2. In order to reduce the errors caused by non-random arrangement, strict randomized layout was implemented. The sequence of tests was determined by means of a computer generating random numbers.

Table 2. Experimental factor-level coding parameters.

Code	Experimental Factor		
	Dynamic–Static Blade Cutting Gap (mm)	Dynamic–Static Blade Cutting Angle (°)	Dynamic Blade Install Angle (°)
−1.682	0.60	5.00	−5.00
−1	0.76	7.03	−2.97
0	1.00	10.00	0
1	1.24	12.97	2.97
1.682	1.40	15.00	5.00

Based on the actual field conditions of the weeding device, the forward velocity of the device was set to 0.6 m/s, the rotational speed to 1.06 rad/s, and the working depth to 40 mm.

2.4.3. Calculation Method for Experimental Metrics

(1) Soil stir rate

The soil stir rate y_1 is defined as the ratio of the number of soil grid units that have experienced a decrease in density due to disruption to the total number of grid units in the composite model soil. In the same composite soil model, a higher soil stir rate indicates a more thorough fluid disturbance by the device, representing a stronger weeding capacity of the device [45]. LS-PrePost 4.3 post-processing software was used to observe the density changes in the fluid domain at different time points and to read the changes in the number of grid units. The data was then exported to Excel for organization and calculation. The calculation formula is given by Equation (14).

$$y_1 = \frac{S_1}{S_2} \times 100\% \quad (14)$$

where y_1 is the soil stir rate (%); S_1 is the number of soil grid units with a reduced density; S_2 is the total number of grid units in the composite model soil.

(2) Coupling stress

Coupling stress y_2 is defined as the average value of the coupling stress generated on the coupling surface during the interaction between the weeding device and the coupled material. In the same composite soil model, a smaller coupling stress indicates that the device experiences a lower resistance and energy consumption during the weeding process [39,46]. LS-PrePost post-processing software was used to observe the stress distribution in the fluid domain at different time points. It can also be intuitively seen in the coupling stress–time curve that the curve fluctuates less, which also means that the coupling stress on the coupling surface is stable and reliable at these times. The stable coupling stress was exported to Excel 2016 (Microsoft, Redmond, WA, USA) for sorting and calculation, and the calculation formula is shown as Equation (15).

$$y_2 = \frac{\sum_{i=1}^n |\sigma_i|}{n} \times 100\% \quad (15)$$

where y_2 is the coupling stress (Mpa); σ_i is the stable coupling stress (Mpa); n is the number of times at which the stable coupling stress is present.

2.5. Field Experiment

2.5.1. Experimental Conditions

The field experiment was conducted from 30 May to 3 June 2023, at Harahai Farm, Meris Daur District, Qiqihar City, Heilongjiang Province, China (123.555° E, 47.664° N), and the soil type was typical northeast sticky black soil. The rice seedlings in the experimental

plots were transplanted on 18 May 2023, and no herbicides were applied. During the experiment, the minimum temperature was 11 °C, the maximum temperature was 25 °C, and there was no rainfall. The water depth in the experimental field ranged from 15 mm to 40 mm, the mud depth was between 150 mm to 200 mm, the height of the rice seedlings ranged from 150 mm to 300 mm, with a row spacing of 300 mm and plant spacing of 150 mm. The average weed density in the experimental plot was measured to be 40 plants/m², with the primary weeds being arrowhead and barnyard grass.

The structural parameters of the combined paddy field inter-row weeding wheel (CW) were rounded off based on the optimized values for ease of processing and assembly: d was set at 1.4 mm, θ at 11.0°, and α at −3.5°. The key specifications of a rat cage bar-type paddy field inter-row weeding wheel (SCW) include a working width of 200 mm and 10 grid bars. The CW and SCW were mounted on the remote-controlled chassis for paddy fields (power 3.6 kW, wheel track width 1.2 m, wheelbase 0.8 m) using bolts. The field experiment setup is shown in Figure 7a.



Figure 7. Field test equipment and operating environment. (a) Field test equipment; (b) Field test environment.

2.5.2. Experimental Method

To investigate the performance of the CW, field comparison trials were conducted using the SCW as a control group, with the weeding rate and seedling damage rate as evaluation criteria, across different working speeds (0.6 m/s, 0.7 m/s, 0.8 m/s, 0.9 m/s, and 1.0 m/s). Each level was repeated three times. A polynomial regression and one-way analysis of variance were used to process the experimental results. The weeding wheel's penetration depth into the soil was set at 40 mm. The chassis was operated by the same person throughout the entire process. The experimental plots in the field were divided into testing zones, each measuring 2 m in length and 200 mm in width (corresponding to the weeding wheel's working width). A 1.5 m buffer zone was established between each testing zone for statistical purposes, as shown in Figure 7b. To reduce errors due to non-random arrangements, the order of the tests is determined by generating random numbers using a computer.

2.5.3. Calculation of Experimental Metrics

Weeds that were floating on the water's surface, buried in the mud, and had their stems cut were defined as removed weeds. Weeds whose root systems remained connected to the mud and could continue to grow after the operation were defined as unremoved weeds. Rice plants that had their leaves pressed down, were uprooted, or were lodged on both sides of the testing zone after the operation were defined as damaged seedlings. The formulas for calculating the weeding rate and seedling damage rate are expressed as (16) and (17):

$$\sigma_1 = \frac{W_0 - W_1}{W_0} \times 100\% \quad (16)$$

$$\sigma_2 = \frac{Y_1}{Y_0} \times 100\% \quad (17)$$

where W_0 is the total number of weeds in the test area before operation; W_1 is the total number of weeds remaining in the test area after operation; σ_1 is the weeding rate (%); Y_0 is the number of seedlings on both sides of the test area before operation; Y_1 is the number of damaged seedlings on both sides of the test area after operation; σ_2 is the seedling damage rate (%).

3. Results and Discussion

3.1. Experimental Results

3.1.1. Results of Weed Cutting Mechanics Tests

A schematic illustration of the geometric parameters of paddy field weeds is shown in Figure 8a, and the geometric parameters of the paddy field weeds collected in this study are provided in Table 3.

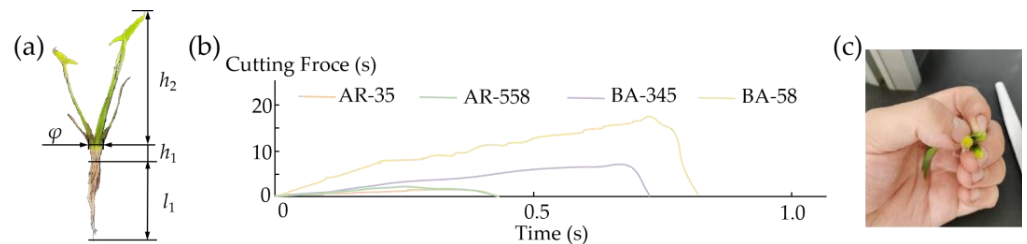


Figure 8. Geometric characteristics and the cutting force–time curve of the paddy field weeds. (a) Geometric parameters of the paddy field weeds; (b) Paddy weed cutting force–time curve; (c) Arrowhead cross-section.

Table 3. Geometric parameters of paddy field weeds.

Weed Species	Average Root Depth of Weeds/ l_1 (mm)	Average Height from Mud Surface to Weed Root/ h_1 (mm)	Average Length of Weed Stalk/ h_2 (mm)	Average Stem Diameter of Weed at Mud Surface/ φ (mm)
BA-345	19.61 ± 6.80	3.72 ± 1.62	62.61 ± 36.03	2.20 ± 0.53
BA-58	39.00 ± 18.70	4.60 ± 1.84	88.90 ± 39.93	3.51 ± 0.72
AR-35	71.75 ± 19.78	4.14 ± 1.70	51.00 ± 24.57	4.50 ± 1.11
AR-558	73.65 ± 17.07	3.50 ± 1.64	80.85 ± 18.04	5.45 ± 1.12

The cutting force–time curves for barnyard grass and arrowhead are depicted in Figure 8b.

Under the same θ conditions, the effect of d on the peak cutting force of weeds is shown in Figure 9a. Polynomial regression analysis reveals that the fitting equations for the peak cutting forces of the blades on BA-345, BA-58, AR-35, AR-558 are as shown in Equation (18). Through variance analysis, the variation in d has no significant effect on the peak cutting force of BA-345, AR-35, and AR-558 ($p > 0.05$). When d varies within the range of 0.2 mm to 1.8 mm, the average peak cutting force of the blade on BA-345 is 5.45 N, on AR-35 is 2.35 N, and on BA-558 is 4.26 N. The peak cutting force of BA-58 increases with an increase in d ($p < 0.05$). The maximum peak cutting force of the blade on BA-58 is 27.07 N, while the minimum is 19.58 N. It was also observed during the experiments that when d increases to 1.8 mm, the cutting location of BA-345 tends to bend but is not easily severed.

$$\begin{cases} y_1 = 0.125x^3 - 0.4402x^2 + 0.5079x + 5.2786, R_1^2 = 0.9221 \\ y_2 = 2.5625x^3 - 5.6607x^2 + 4.0389x + 20.454, R_2^2 = 0.9895 \\ y_3 = 0.0755x^3 + 0.3386x^2 - 1.2384x + 2.9542, R_3^2 = 0.9438 \\ y_4 = -0.0469x^3 + 0.1299x^2 - 0.2117x + 4.3933, R_4^2 = 0.9903 \end{cases} \quad (18)$$

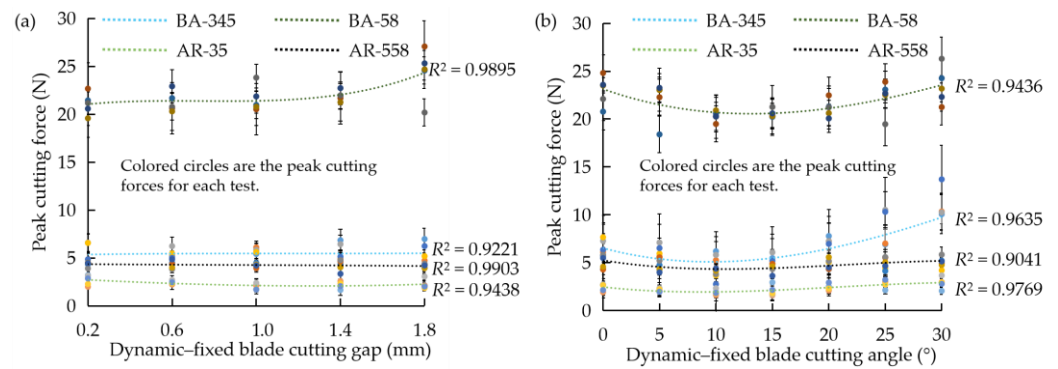


Figure 9. Experimental results of weed cutting mechanical characteristics. (a) Effect of dynamic-fixed blade cutting gap on the peak cutting force of paddy weeds; (b) Effect of dynamic-fixed blade cutting angle on the peak cutting force of paddy weeds.

Under the same d conditions, the effect of θ on the peak cutting force of weeds is shown in Figure 9b. Polynomial regression analysis reveals that the fitting equations for the peak cutting forces of the blades on BA-345, BA-58, AR-35, AR-558 are as shown in Equation (19). The peak cutting force for all four weed types initially decreases and then increases with an increase in the cutting angle, and the minimum peak cutting force occurs within the range of 5° to 15° . Through variance analysis, θ has a highly significant effect on the peak cutting force of BA-345, BA-58, and AR-35 ($p \leq 0.01$), and a significant effect on the peak cutting force of AR-558 ($p < 0.05$). The maximum peak cutting force of the blade on BA-345 is 13.71 N, while the minimum is 2.77 N; on BA-58, it is 26.30 N (maximum) and 18.40 N (minimum); on AR-35, it is 3.68 N (maximum) and 1.62 N (minimum); on AR-558, it is 5.85 N (maximum) and 3.64 N (minimum).

$$\begin{cases} y_5 = -0.0002x^3 + 0.0185x^2 - 0.3119x + 6.521, R_5^2 = 0.9635 \\ y_6 = -0.0001x^3 + 0.0186x^2 - 0.4155x + 23.13, R_6^2 = 0.9436 \\ y_7 = -0.0002x^3 + 0.0093x^2 - 0.1288x + 2.4656, R_7^2 = 0.9769 \\ y_8 = -0.0002x^3 + 0.0118x^2 - 0.1901x + 5.2503, R_8^2 = 0.9041 \end{cases} \quad (19)$$

3.1.2. Results of Simulation Tests

The results of the simulation tests are presented in Table 4, where x_1 , x_2 , and x_3 correspond to the coded values of the dynamic-fixed blade cutting gap, dynamic-fixed blade cutting angle, and the dynamic blade install angle, respectively.

Using Design-Expert 8.0.6 Software, a regression analysis and ANOVA were performed on the data. The regression equations for the soil stir rate and coupling stress are shown in Equations (20) and (21). The results of the variance analysis are presented in Table 5.

$$y_1 = 35.34 - 0.1155x_1 + 3.31x_2 - 0.4711x_3 - 0.2237x_1x_2 - 0.0887x_1x_3 - 0.9487x_2x_3 + 1.92x_1^2 + 0.0611x_2^2 + 0.1813x_3^2 \quad (20)$$

$$y_2 = 0.0249 - 0.0004x_1 - 0.0007x_2 + 0.0091x_3 - 0.0001x_1x_2 + 0.0006x_1x_3 - 0.0035x_2x_3 - 0.0007x_1^2 + 0.0012x_2^2 + 0.0037x_3^2 \quad (21)$$

Table 4. Simulation test plan and results.

Experiment No.	Experimental Factors			Performance Indicators	
	Dynamic-Fixed Blade Cutting Gap x_1 (mm)	Dynamic-Fixed Blade Cutting Angle x_2 (°)	Dynamic Blade Install Angle x_3 (°)	Soil Stir Rate (%)	Coupling Stress (Pa)
1	−1	−1	−1	34.13	17,020
2	1	−1	−1	34.05	17,140
3	−1	1	−1	42.48	24,050
4	1	1	−1	42.53	21,710
5	−1	−1	1	34.47	41,980
6	1	−1	1	35.06	42,410
7	−1	1	1	40.05	32,980
8	1	1	1	38.72	34,830
9	−1.682	0	0	40.73	24,640
10	1.682	0	0	40.25	21,720
11	0	−1.682	0	29.56	29,860
12	0	1.682	0	40.92	27,080
13	0	0	−1.682	36.04	20,020
14	0	0	1.682	35.12	50,900
15	0	0	0	35.26	24,710
16	0	0	0	35.36	24,820
17	0	0	0	35.74	25,130
18	0	0	0	34.66	25,810
19	0	0	0	34.97	24,240
20	0	0	0	36.12	24,590

Table 5. Variance analysis of regression equations.

Source of Variance	Soil Stir Rate						Coupling Stress					
	Sum of Squares	Degrees of Freedom	Mean Square	F	p	Significance	Sum of Squares	Degrees of Freedom	Mean Square	F	p	Significance
Model	213.53	9	23.73	77.63	<0.0001	**	0.15×10^{-2}	9	0.02×10^{-2}	257.21	<0.0001	**
x_1	0.18	1	0.18	0.60	0.46		1.72×10^{-6}	1	1.72×10^{-6}	2.72	0.13	
x_2	149.43	1	149.43	488.93	<0.0001	**	6.83×10^{-6}	1	6.82×10^{-6}	10.80	0.0082	**
x_3	3.03	1	3.03	9.93	0.0103	*	0.11×10^{-2}	1	0.11×10^{-2}	1786.67	<0.0001	**
x_1x_2	0.40	1	0.40	1.31	0.279		1.35×10^{-7}	1	1.35×10^{-7}	0.2138	0.65	
x_1x_3	0.06	1	0.06	0.21	0.6595		2.53×10^{-6}	1	2.53×10^{-6}	4.00	0.0733	
x_2x_3	7.20	1	7.20	23.56	0.0007	**	0.01×10^{-2}	1	0.01×10^{-2}	156.98	<0.0001	**
x_1^2	52.97	1	52.97	177.33	<0.0001	**	6.28×10^{-6}	1	6.28×10^{-6}	9.93	0.0103	*
x_2^2	0.05	1	0.05	0.18	0.6836		0	1	0	33.39	0.0002	**
x_3^2	0.47	1	0.47	1.55	0.2415		0.02×10^{-2}	1	0.02×10^{-2}	308.92	<0.0001	**
Residual	3.06	10	0.31				6.32×10^{-6}	10	6.32×10^{-7}			
Misfit term	1.68	5	0.34	1.22	0.41		4.87×10^{-6}	5	9.74×10^{-7}	3.35	0.1053	
Pure error	1.37	5	0.27				1.45×10^{-6}	5	2.91×10^{-7}			
Total	216.59	19					0.15×10^{-2}	19				

Note: * indicates significance ($0.01 < p < 0.05$), ** indicates highly significant ($p \leq 0.01$); x_1 is the dynamic-fixed blade cutting gap, x_2 is the dynamic-fixed blade cutting angle, and x_3 is the dynamic blade install angle.

The ANOVA of the regression equations reveals that the regression models for the soil stir rate and coupling stress of the weeding wheel are highly significant ($p \leq 0.01$), with non-significant lack-of-fit terms ($p > 0.05$). The coefficient of determination R^2 for the soil stir rate model was 0.986, and the R^2 for the coupling stress model was 0.996, indicating the good fit of the regression equations.

The significance of each factor can be determined by comparing the p -values in Table 5. For the soil stir rate, the dynamic-fixed blade cutting angle x_2 has a highly significant effect ($p \leq 0.01$), the dynamic blade install angle x_3 has a significant effect ($p < 0.05$), and

the interaction term x_2x_3 has a highly significant effect ($p \leq 0.01$); for coupling stress, the dynamic-fixed blade cutting angle x_2 has a highly significant effect ($p \leq 0.01$), the dynamic blade install angle has a highly significant effect ($p \leq 0.01$), and the interaction term x_2x_3 has a highly significant effect ($p \leq 0.01$). The response surface of the interactive factors on the soil disturbance rate and coupling stress is shown in Figure 10.

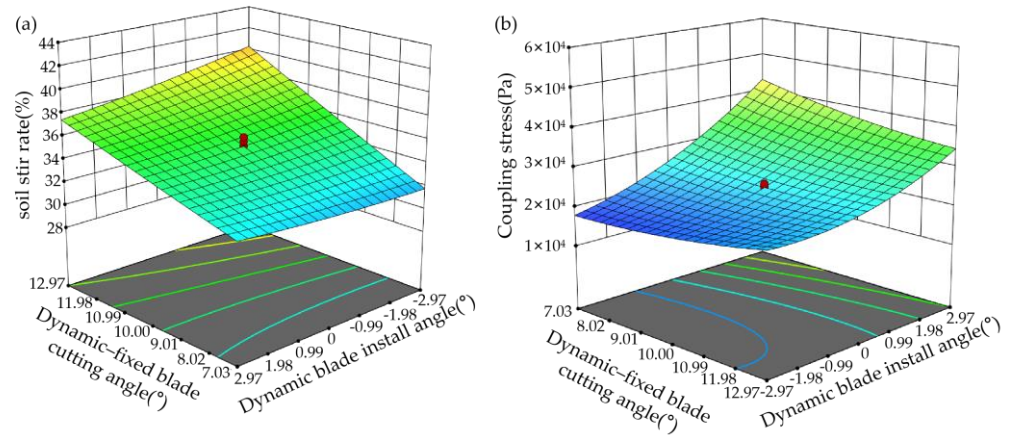


Figure 10. Response surface of the interaction effects on the soil stir rate and coupling stress. (a) Interaction effects on the soil stir rate; (b) Interaction effects on coupling stress.

An analysis is conducted on the impact of the interaction term x_2x_3 on the soil stir rate and coupling stress. As the dynamic-fixed blade cutting angle increases, both the soil stir rate and the coupling stress increase. This is because the increased dynamic-fixed blade cutting angle enlarges the area of action on the soil for each dynamic blade and pre-fixed blade, leading to an increase in both the soil stir rate and coupling stress. With an increase in the dynamic blade install angle, the soil stir rate decreases slightly, but not significantly. This is because the change in the dynamic blade install angle within a small range does not have a significant effect on the soil stir rate. The coupling stress shows an increasing trend with an increase in the dynamic blade install angle. This is because a smaller dynamic blade install angle allows the dynamic blade to penetrate the soil at a certain angle during rotation. As the dynamic blade install angle increases beyond 0°, the dynamic blade shifts from its penetration into the soil to pressing into the soil, leading to an increase in the coupling stress. This observation aligns with the findings of Zhang et al. [22].

To obtain the optimal structural parameter combination for this inter-row weeding device, with the final optimization objectives of maximizing the soil stir rate and minimizing coupling stress, a non-linear programming parameter model was established using the Optimization function in Design-Expert 8.0.6, taking into account the experimental factor boundary conditions [47], as shown in Equation (22).

$$\begin{cases} \max y_1 \\ \min y_2 \\ \text{s.t.} \begin{cases} 0.6\text{mm} \leq x_1 \leq 1.4\text{mm} \\ 5^\circ \leq x_2 \leq 15^\circ \\ -5^\circ \leq x_3 \leq 5^\circ \end{cases} \end{cases} \quad (22)$$

One set of the optimal structural parameter combinations for the weeding device was selected from the optimization objectives: a dynamic-fixed blade cutting gap of 1.4 mm, a dynamic-fixed blade cutting angle of 10.95°, and a dynamic blade install angle of -3.44°, resulting in a soil stir rate of 42.73% and coupling stress of 17,000 Pa. Based on the optimization results, a simulation verification was conducted, resulting in a soil

stir rate of 42.86% and coupling stress of 17,020 Pa, which is in close agreement with the optimization results.

3.1.3. Field Experiment Results

The field experiment results were processed and analyzed using Excel 2016 software. The effect of the working speed on the weeding rate and seedling damage rate for two types of weeding wheels is shown in Figure 10. Given the non-linear nature of the data, a polynomial regression analysis was employed to obtain the following fitting equation, as shown in Equation (23).

$$\begin{cases} y_1 = -56.452x^2 + 95.32x + 33.348, R_1^2 = 0.972 \\ y_2 = -56.452x^2 + 147.79x + 31.837, R_2^2 = 0.979 \\ y_3 = 16.667x^2 - 14.733x + 2.7, R_3^2 = 0.918 \\ y_4 = 33.333x^2 - 39.067x + 11.4, R_4^2 = 0.925 \end{cases} \quad (23)$$

As can be seen from Figure 11, the weeding rates for the CW (combined paddy field inter-row weeding wheel) and the SCW (rat cage bar-type paddy field inter-row weeding wheel) exhibit a trend of increasing and then decreasing as the working speed increases, while the seedling damage rate increases with the working speed. The effect of different advance speeds on the weeding rate of the CW is highly significant ($p \leq 0.01$), and the effect on the seedling damage rate of the CW is significant ($p < 0.05$). The average weeding rate of the CW is 89.7%, and the average seedling damage rate is 2.2%. The effect of different advance speeds on the weeding rate of the SCW is highly significant ($p \leq 0.01$), and the effect on the seedling damage rate of the SCW is significant ($p \leq 0.01$). The average weeding rate of the SCW is 72.3%, and the average seedling damage rate is 2.4%. When compared to the SCW, the CW exhibits a significantly higher average weeding rate ($p \leq 0.01$), with no significant difference in the average seedling damage rate ($p > 0.05$) between the CW and the SCW.

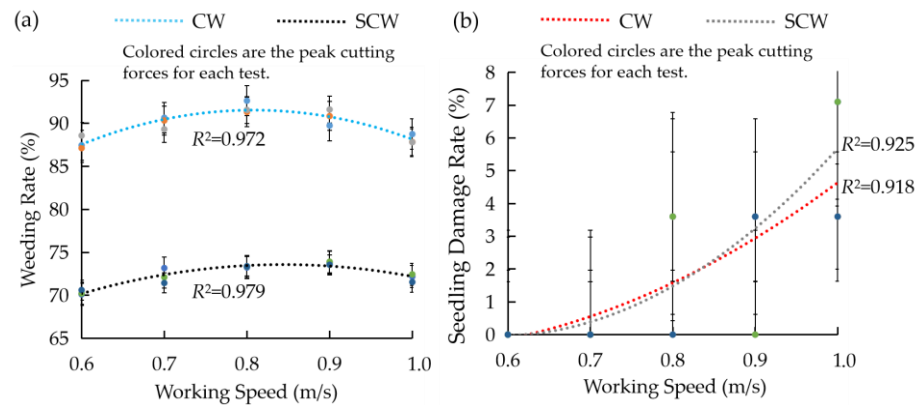


Figure 11. Field test results. (a) The trend of weeding rate variation with the speed for two types of weeding wheels; (b) The trend of seedling damage rate variation with the speed for two types of weeding wheels.

3.2. Discussion

3.2.1. Discussion of Weed Cutting Mechanics Test Results

Based on the measurement results and field surveys, barnyard grass and arrowhead were the predominant weeds in the rice fields after transplanting. Additionally, even within the same period and plot, the growth of weeds can vary. This variation is due to the different effects of temperature, light intensity, and seed damage on seed germination rates, as well as the effect of factors like soil moisture on weeds [48,49]. These factors result in variations in the geometric parameters of the weeds.

During the experiments, no adhesion or irregularities were observed on the cross-sections of the weeds. As shown in Figure 8b, the trends in cutting force versus time for barnyard grass and arrowhead are roughly similar. While the cutting forces observed in this study differ from those for cutting other crops, the overall trend of the cutting force–time curve is generally consistent [50]. The cutting process can be divided into three stages: compression, compression-cutting, and cutting. When the blade first contacts the weed stem, it exerts a compressive force on the stem. With increasing cutting time, the cutting area on the stem undergoes plastic deformation. When the deformation exceeds the limit of the stem material, the blade damages the stem and subsequently severs the weed's roots. During the cutting stage, as cutting time increases, more fibers are cut, resulting in a reduction in stem strength and a gradual decrease in cutting force. The peak cutting force for barnyard grass is greater than that for arrowhead, and the cutting time is longer. This is because arrowhead has a lower internal stem density, while barnyard grass has a higher degree of lignification in its stem, resulting in a higher elastic modulus and a greater cross-sectional moment of inertia [46]. Therefore, more compressive force and longer compression time are required to cut barnyard grass.

BA-345 has a lower degree of stem lignification and a lower root strength. Additionally, observations of the cutting cross-section of arrowhead reveal that arrowhead stems are composed of various branches, as shown in Figure 8c. The main root formed by these branches is not dense and has low fragility. Hence, small variations in the dynamic–fixed blade cutting gap have no significant effect on the peak cutting forces of AR-35, AR-558, and BA-345. BA-58 has a higher degree of stem lignification, resulting in greater stem fragility. These large-leaved barnyard grasses can be considered a simply supported beam model fixed at both ends during the cutting process. These types of barnyard grasses have a constant shear force and bending moment on the same cross-section. As the dynamic–fixed blade cutting gap increases, the force exerted by the blade on the weed stem increases, consistent with the theoretical analysis of the structural design mentioned earlier.

When θ is 0° , the blade edge direction is parallel to the cutting direction, and the blade edge is perpendicular to the weed stem axis, representing a transverse cut within the normal cutting. As θ increases, the weed stem axis intersects obliquely with the blade edge direction and is perpendicular to the cutting direction, representing an oblique cut within the normal cutting [51]. Due to the anisotropic viscoelasticity of weed stems, within a certain range of angles, oblique cutting can tear the weed's fiber structure and reduce its cohesion, making it require less cutting force than transverse cutting at 0° . Consequently, the peak cutting force of weeds decreases with an increasing θ . However, as θ continues to increase, the cross-sectional area of the weed stem cut by the blade also increases. This effect becomes more significant than the reduction in fiber cohesion, leading to an increase in the average peak cutting force. This phenomenon aligns with the research conducted by Igathinathane et al. [52].

Considering the constraints of the device structure, d cannot be too small. Therefore, the range of d values in the simulation tests was set from 0.6 to 1.4 mm, and the range of θ was set from 5° to 15° .

3.2.2. Discussion of Simulation Test Results

This section analyzes the simulation process. The cloud maps of the fluid density at different time intervals are depicted in Figure 12a–d. As the weeding wheel rotates and moves forward, the pressure generated by the contact between the dynamic and fixed knives and the soil causes damage to the soil, resulting in the displacement of soil particles. Water from the water layer flows into the damaged space and couples with the soil unit, hence, the fluid density decreases. An analysis of the simulation process reveals the following: At the initial moment, when the device first makes contact with the coupling material, only a small portion of the coupling material is disturbed, resulting in a slight decrease in fluid density. As the device continues to move forward, the dynamic blade and fixed blade agitate the coupling material, causing the most significant decrease in density

within the region where the dynamic–fixed blade is acting. When the device continues to move forward, the fluid density further away from the device gradually increases. This is because the device stirs the soil, causing the initially compacted soil to be disrupted, leading to a decrease in density. As the device advances, the fluid further away from the device experiences reduced disturbance, gradually allowing the density to recover.

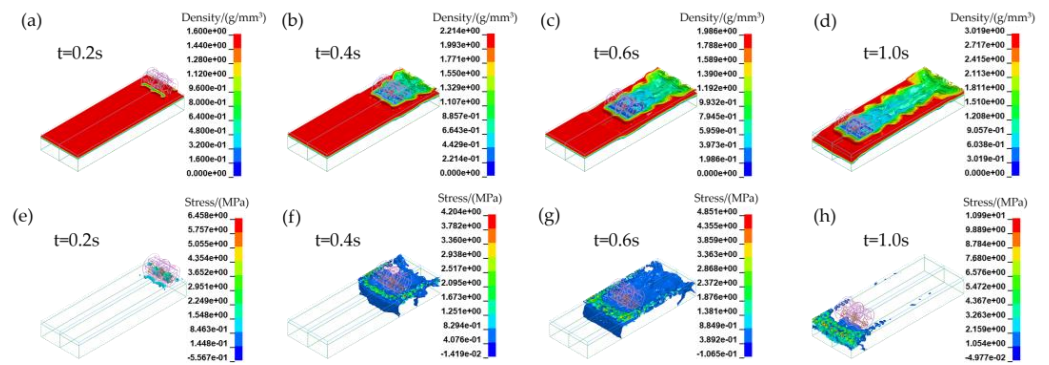


Figure 12. Density vs. coupling stress cloud maps at different time intervals. (a–d) Density cloud maps at different time intervals; (e–h) Coupling stress cloud maps at different time intervals.

The cloud maps of coupling stress at different time intervals are shown in Figure 12e–h. After the dynamic-blade is inserted into the soil, the blade compresses and pulls on the soil. Therefore, the coupling stress is both positive and negative. The analysis of the simulation process reveals the following: At the initial moment, when the device first comes into contact with the coupling material, only a small area is affected by the force exerted by the device. As the device advances, the rear-fixed blade is located below the soil layer, exerting force on the soil beneath the device. During the device’s forward movement and the rotation of the dynamic blade, there is mutual compression between the blade and the soil, as well as between adjacent soil particles. This results in the generation of forces. Since the dynamic blades are uniformly distributed on the dynamic blade disk, each dynamic blade enters and exits the soil successively during the rotation of the dynamic blade disk. Consequently, coupling stress exhibits a pulsating pattern.

3.2.3. Discussion of Field Test Results

The operational performance of the two weeding wheels is depicted in Figure 13. During the experiments, it was observed that the CW exhibited no significant clogging issues, while the SCW experienced severe clogging, with the CW achieving a superior level of weed fragmentation.

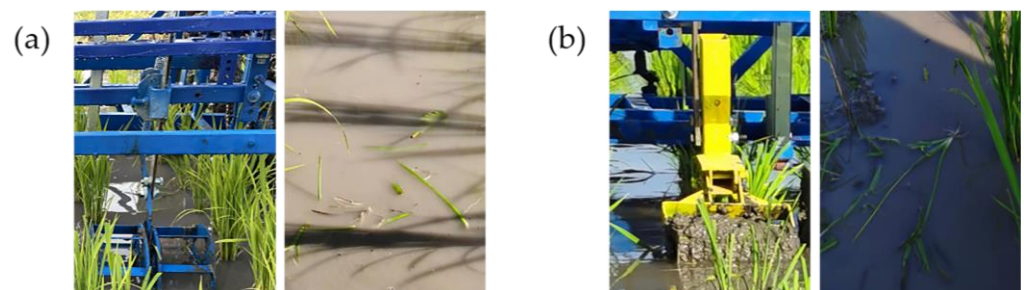


Figure 13. Operating performances of the CW and SCW. (a) The CW’s operating performance; (b) the SCW’s operating performance.

Analysis of the experimental observations and results reveals several key insights. At lower working speeds, the CW’s dynamic blade and fixed blade have a smaller relative movement speed, making it less effective at removing weeds. As the working speed increases, the relative speed between the dynamic blade and the fixed blade also increases,

making it easier to cut weeds. Therefore, the weeding rate of the CW first showed an increasing trend. However, when the working speed continues to increase, the CW experiences sliding behavior [53]. At this point, the relative speed between the dynamic and fixed blades decreases, sometimes even leading to a relative standstill, resulting in a decrease in weeding efficiency. Therefore, at this time, the weeding rate shows a decreasing trend with the increase of the working speed. The increased working speed also disturbs the soil in the non-weeding zone, causing seedlings to be overturned and increasing the injury rate, in alignment with findings from Wang et al. [54].

At lower forward speeds, the SCW has minimal soil disturbance, making it less effective at weed removal. As the working speed increases, the SCW's soil disturbance increases, aiding weed removal. Therefore, the weeding rate of the SCW also first showed an increasing trend. However, when the working speed continues to increase, the SCW experiences severe clogging. The adhering mud transforms the SCW, which has rows of bars, into a cylindrical shape, reducing the pressure and pulling effect on weeds and consequently decreasing the weeding rate. At this point, the weeding rate of the SCW decreases as the working speed increases. As the working speed of the SCW increases, the soil disturbance rate also rises, which damages the soil in the seedling avoidance area, and the increase in working speed likewise leads to a higher rate of seedling damage.

In summary, due to its dynamic–fixed cutting relationship, the CW experiences reduced clogging. It combines the functions of pressing, burying, and shredding weeds. The fragmented weeds are more likely to float on the water's surface, which may explain the higher average weeding rate of the CW. The CW achieves a 17.4% higher average weeding rate compared to traditional devices. A comparison between field test results and simulation test results indicates that greater soil disturbance results in better weeding effectiveness, validating the feasibility of the simulation tests. Both weeding devices have approximately the same working width, which is smaller than the spacing between rice seedlings. Therefore, under similar driving techniques, the two weeding wheels do not significantly differ in seedling injury rates.

The CW designed in this study is structurally similar to the conventional SCW and is not powered. While it replaces the tine of the SCW with a dynamic blade and modifies the installation angle and quantity of the dynamic blade, it also adds a fixed-blade structure to the CW's fixed shaft. However, the overall manufacturing complexity and production cost only increase slightly. This suggests that a small increase in manufacturing cost can yield significant benefits. Therefore, it is recommended to use the CW instead of the conventional SCW for inter-row weeding in rice fields to improve weeding rates and weed mortality rates.

Future work will involve further improvements to the device to enhance its ability to shred weeds, thereby increasing weed mortality rates. Large-scale field trials will also be conducted to validate the device's reliability in real farm conditions.

4. Conclusions

In this paper, a combined paddy field inter-row weeding wheel is designed. On the basis of the theoretical analysis and experiments of weed cutting's mechanical characteristics, its dynamic–static blade cutting gap, dynamic–static blade cutting angle, and dynamic blade install angle are optimized based on display dynamics. A field comparative experiment was conducted to verify the operational effectiveness of the combined paddy field inter-row weeding wheel. The conclusions drawn are as follows:

- (1) Theoretical analysis of the operational process of the designed combination weeding wheel led to the determination of certain parameters: $h = 40$ mm, $B = 200$ mm, $R_1 = 90$ mm, $R_2 = 70$ mm, $Z = 7$, and $d_1 = 63$ mm.
- (2) A single factor test on the mechanical properties of weed cutting was carried out. The results show that d has a significant effect on the peak cutting force of BA-58, but no significant effect on the peak cutting force of BA-345, AR-35, and AR-558. Within the range of d from 0.6 to 1.4 mm, the peak cutting force on BA-58 reached its minimum.

θ has a highly significant effect on the peak cutting force of BA-345, BA-58, and AR-35, and has a significant effect on the peak cutting force of AR-558. Within the range of θ from 5 to 15°, the peak cutting force on the above four weeds appeared to be the minimum.

- (3) A coupled simulation model of the weeding wheel–soil–water FSI was established using explicit dynamics simulation technology (LS-DYNA). A three-factor, five-level simulation test based on the central composite experimental design principle was conducted. The optimal structural parameters for the device were determined to be the following: d is 1.4 mm, θ is 10.95°, and α is -3.44° .
- (4) A comparative field experiment was conducted between the CW and SCW. The results revealed that the average weeding rate of the CW was 89.7%, and the seedling injury rate was 2.2%. The average weeding rate of the SCW was 72.3%, and the average seedling injury rate was 2.4%. The average weeding rate of the CW was significantly more outperforming than that of the SCW, and there was no significant difference in the average seedling injury rate between the CW and SCW.

Author Contributions: Conceptualization, J.W., Q.W. and Y.-J.W.; methodology, J.W., Q.W., Y.-J.W. and Z.L.; software, J.W. and Q.W.; validation, Z.L. and M.Y.; formal analysis, W.Z. and L.Q.; investigation, J.W. and Q.W.; resources, Q.W. and J.W.; data curation, J.W., Q.W. and Z.L.; writing—original draft preparation, J.W. and Q.W.; writing—review and editing, J.W., Q.W., Z.L. and H.T.; visualization, J.W. and H.T.; supervision, J.W.; project administration, Y.-J.W. and J.W.; funding acquisition, J.W. and Y.-J.W. All authors have read and agreed to the published version of the manuscript.

Funding: This research was financially supported by the National Science Foundation of China (U23A20174), Heilongjiang Provincial Key Research and Development Program (No. 2023ZX05B01) and the Industrial Technology System of National Rice (CARS-01).

Institutional Review Board Statement: Not applicable.

Data Availability Statement: Data are contained within the article.

Acknowledgments: The authors would like to thank their schools and colleges, as well as the funding providers of the project. All support and assistance is sincerely appreciated.

Conflicts of Interest: The authors declare no conflicts of interest.

References

1. Birla, D.S.; Malik, K.; Sainger, M.; Chaudhary, D.; Jaiwal, R.; Jaiwal, P.K. Progress and Challenges in Improving the Nutritional Quality of Rice (*Oryza sativa* L.). *Crit. Rev. Food Sci. Nutr.* **2017**, *57*, 2455–2481. [[CrossRef](#)]
2. Sen, S.; Chakraborty, R.; Kalita, P. Rice—Not Just a Staple Food: A Comprehensive Review on Its Phytochemicals and Therapeutic Potential. *Trends Food Sci. Technol.* **2020**, *97*, 265–285. [[CrossRef](#)]
3. Young, S.L.; Anderson, J.V.; Baerson, S.R.; Bajsa-Hirschel, J.; Blumenthal, D.M.; Boyd, C.S.; Boyette, C.D.; Brennan, E.B.; Cantrell, C.L.; Chao, W.S.; et al. Agricultural Research Service Weed Science Research: Past, Present, and Future. *Weed Sci.* **2023**, *71*, 312–327. [[CrossRef](#)]
4. Ragesh, K.T.; Jogdand, S.V.; Victor, V.M. Field Performance Evaluation of Power Weeder for Paddy Crop. *Curr. Agric. Res. J.* **2018**, *6*, 441–448. [[CrossRef](#)]
5. Bennett, A.J.; Yadav, R.; Jha, P. Using Soybean Chaff Lining to Manage Waterhemp (*Amaranthus tuberculatus*) in a Soybean–Corn Rotation. *Weed Sci.* **2023**, *71*, 395–402. [[CrossRef](#)]
6. Domingo, C.; San Segundo, B. Rice Thematic Special Issue: Beneficial Plant–Microbe Interactions in Rice. *Rice* **2023**, *16*, 50. [[CrossRef](#)] [[PubMed](#)]
7. Hasanuzzaman, M.; Mohsin, S.M.; Bhuyan, M.H.M.B.; Bhuiyan, T.F.; Anee, T.I.; Masud, A.A.C.; Nahar, K. Phytotoxicity, Environmental and Health Hazards of Herbicides: Challenges and Ways Forward. In *Agrochemicals Detection, Treatment and Remediation*; Elsevier: Amsterdam, The Netherlands, 2020; pp. 55–99.
8. Zeng, Z.; Martin, A.; Chen, Y.; Ma, X. Weeding Performance of a Spring-Tine Harrow as Affected by Timing and Operational Parameters. *Weed Sci.* **2021**, *69*, 247–256. [[CrossRef](#)]
9. Shaner, D.L.; Beckie, H.J. The Future for Weed Control and Technology. *Pest Manag. Sci.* **2014**, *70*, 1329–1339. [[CrossRef](#)] [[PubMed](#)]
10. Ranji, A.; Parashkoochi, M.G.; Zamani, D.M.; Ghahderijani, M. Evaluation of Agronomic, Technical, Economic, and Environmental Issues by Analytic Hierarchy Process for Rice Weeding Machine. *Energy Rep.* **2022**, *8*, 774–783. [[CrossRef](#)]
11. Liu, C.; Yang, K.; Chen, Y.; Gong, H.; Feng, X.; Tang, Z.; Fu, D.; Qi, L. Benefits of Mechanical Weeding for Weed Control, Rice Growth Characteristics and Yield in Paddy Fields. *Field Crops Res.* **2023**, *293*, 108852. [[CrossRef](#)]

12. Pareja, L.; Pérez-Parada, A.; Agüera, A.; Cesio, V.; Heinzen, H.; Fernández-Alba, A.R. Photolytic and Photocatalytic Degradation of Quinclorac in Ultrapure and Paddy Field Water: Identification of Transformation Products and Pathways. *Chemosphere* **2012**, *87*, 838–844. [[CrossRef](#)]
13. Jones, E.A.L.; Austin, R.; Dunne, J.C.; Leon, R.G.; Everman, W.J. Discrimination between Protoporphyrinogen Oxidase-Inhibiting Herbicide-Resistant and Herbicide-Susceptible Redroot Pigweed (*Amaranthus retroflexus*) with Spectral Reflectance. *Weed Sci.* **2023**, *71*, 198–205. [[CrossRef](#)]
14. Dayan, F.E.; Howell, J.; Marais, J.P.; Ferreira, D.; Koivunen, M. Manuka Oil, A Natural Herbicide with Preemergence Activity. *Weed Sci.* **2011**, *59*, 464–469. [[CrossRef](#)]
15. Owen, M.D.K. Diverse Approaches to Herbicide-Resistant Weed Management. *Weed Sci.* **2016**, *64*, 570–584. [[CrossRef](#)]
16. Richard, D.; Leimbrock-Rosch, L.; Keßler, S.; Stoll, E.; Zimmer, S. Soybean Yield Response to Different Mechanical Weed Control Methods in Organic Agriculture in Luxembourg. *Eur. J. Agron.* **2023**, *147*, 126842. [[CrossRef](#)]
17. Cordill, C.; Grift, T.E. Design and Testing of an Intra-Row Mechanical Weeding Machine for Corn. *Biosyst. Eng.* **2011**, *110*, 247–252. [[CrossRef](#)]
18. Gao, Y.; Zhu, Y.; Zhang, Y.; Zhang, Y.; Wang, Y.; Wang, Z.; Chen, H.; Zhang, Y.; Xiang, J. Physiological Characteristics of Root Regeneration in Rice Seedlings. *Agronomy* **2023**, *13*, 1772. [[CrossRef](#)]
19. Qi, L.; Zhao, L.; Ma, X.; Cui, H.; Zheng, W.; Lu, Y. Design and Experiment of 3GY-1920 Wide-Swath Type Weeding-Cultivating Machine for Paddy. *Trans. Chin. Soc. Agric. Eng.* **2017**, *33*, 47–55. [[CrossRef](#)]
20. Wang, J.; Gao, G.; Yan, D.; Wang, J.; Weng, W.; Chen, B. Design and Experiment of Electric Control Double Row Deep Fertilizing Weeder in Paddy Field. *Trans. Chin. Soc. Agric. Mach.* **2018**, *49*, 46–57.
21. Wang, J.; Weng, W.; Ju, J.; Chen, X.; Wang, J.; Wang, H. Design and Experiment of Weeder between Rows in Rice Field Based on Remote Control Steering. *Trans. Chin. Soc. Agric. Mach.* **2021**, *52*, 97–105.
22. Zhang, Y.; Tian, L.; Cao, C.; Zhu, C.; Qin, K.; Ge, J. Optimization and Validation of Blade Parameters for Inter-Row Weeding Wheel in Paddy Fields. *Front. Plant Sci.* **2022**, *13*, 1003471. [[CrossRef](#)]
23. Kurstjens, D.A.G.; Kropff, M.J. The Impact of Uprooting and Soil-covering on the Effectiveness of Weed Harrowing. *Weed Res.* **2001**, *41*, 211–228. [[CrossRef](#)]
24. Soleimani, N.; Kamandar, M.R.; Khoshnam, F.; Soleimani, A. Defining and Modelling Sesame Stalk Shear Behaviour in Harvesting by Reciprocating Cutting Blade. *Biosyst. Eng.* **2023**, *229*, 44–56. [[CrossRef](#)]
25. Chattopadhyay, P.S.; Pandey, K.P. Effect of Knife and Operational Parameters on Energy Requirement in Flail Forage Harvesting. *J. Agric. Eng. Res.* **1999**, *73*, 3–12. [[CrossRef](#)]
26. Allameh, A.; Reza Alizadeh, M. Specific Cutting Energy Variations under Different Rice Stem Cultivars and Blade Parameters. *Idesia* **2016**, *34*, 11–17. [[CrossRef](#)]
27. Song, S.; Zhou, H.; Xu, L.; Jia, Z.; Hu, G. Cutting Mechanical Properties of Sisal Leaves under Rotary Impact Cutting. *Ind. Crops Prod.* **2022**, *182*, 114856. [[CrossRef](#)]
28. Aydın, İ.; Arslan, S. Mechanical Properties of Cotton Shoots for Topping. *Ind. Crops Prod.* **2018**, *112*, 396–401. [[CrossRef](#)]
29. Ramesh, K. Weed Problems, Ecology, and Management Options in Conservation Agriculture: Issues and Perspectives. *Adv. Agron.* **2015**, *131*, 251–303.
30. Shinde, Y.A.; Jagtap, M.P.; Patil, M.G.; Khatri, N. Experimental Investigation on the Effect of Soil Solarization Incorporating Black, Silver, and Transparent Polythene, and Straw as Mulch, on the Microbial Population and Weed Growth. *Chemosphere* **2023**, *336*, 139263. [[CrossRef](#)]
31. Sadek, M.A.; Chen, Y.; Zeng, Z. Draft Force Prediction for a High-Speed Disc Implement Using Discrete Element Modelling. *Biosyst. Eng.* **2021**, *202*, 133–141. [[CrossRef](#)]
32. Wang, Y.; Xue, W.; Ma, Y.; Tong, J.; Liu, X.; Sun, J. DEM and Soil Bin Study on a Biomimetic Disc Furrow Opener. *Comput. Electron. Agric.* **2019**, *156*, 209–216. [[CrossRef](#)]
33. Aikins, K.A.; Antille, D.L.; Ucgul, M.; Barr, J.B.; Jensen, T.A.; Desbiolles, J.M.A. Analysis of Effects of Operating Speed and Depth on Bentleg Opener Performance in Cohesive Soil Using the Discrete Element Method. *Comput. Electron. Agric.* **2021**, *187*, 106236. [[CrossRef](#)]
34. Wang, Q.; Zhou, W.; Tang, H.; Ma, X.; Wang, J.; Tong, T. Design and Experiment of Arc-Tooth Reciprocating Motion Type Seedling Avoided Weeding Control Device for Intertillage Paddy. *Trans. Chin. Soc. Agric. Mach.* **2021**, *52*, 53–61+72.
35. Zhou, W.; Song, K.; Sun, X.; Fu, Q.; Wang, Y.; Wang, Q.; Yan, D. Design Optimization and Mechanism Analysis of Water Jet-Type Inter-Plant Weeding Device for Water Fields. *Agronomy* **2023**, *13*, 1305. [[CrossRef](#)]
36. Fragassa, C.; Topalovic, M.; Pavlovic, A.; Vulovic, S. Dealing with the Effect of Air in Fluid Structure Interaction by Coupled SPH-FEM Methods. *Materials* **2019**, *12*, 1162. [[CrossRef](#)] [[PubMed](#)]
37. Rokhy, H.; Mostofi, T.M. Tracking the Explosion Characteristics of the Hydrogen-Air Mixture near a Concrete Barrier Wall Using CESE IBM FSI Solver in LS-DYNA Incorporating the Reduced Chemical Kinetic Model. *Int. J. Impact Eng.* **2023**, *172*, 104401. [[CrossRef](#)]
38. Wang, J.; Wang, J.; Yan, D.; Tang, H.; Zhou, W. Design and Experiment of 3SCJ-2 Type Row Weeding Machine for Paddy Field. *Trans. Chin. Soc. Agric. Mach.* **2017**, *48*, 71–78+202.
39. Wang, J.; Ma, X.; Tang, H.; Wang, Q.; Wu, Y.; Zhang, Z. Design and Experiment of Curved-Tooth Oblique Type Inter-Row Weeding Device for Paddy Field. *Trans. Chin. Soc. Agric. Mach.* **2021**, *92*, 91–100.

40. Gaofeng, X.; Shicai, S.; Fudou, Z.; Yun, Z.; Hisashi, K.-N.; David, R.C. Relationship Between Allelopathic Effects and Functional Traits of Different Allelopathic Potential Rice Accessions at Different Growth Stages. *Rice Sci.* **2018**, *25*, 32–41. [[CrossRef](#)]
41. Gibson, K.D.; Breen, J.L.; Hill, J.E.; Caton, B.P.; Foin, T.C. California Arrowhead Is a Weak Competitor in Water-Seeded Rice. *Weed Sci.* **2017**, *49*, 381–384. [[CrossRef](#)]
42. Quan, L.; Wu, B.; Mao, S.; Yang, C.; Li, H. An Instance Segmentation-Based Method to Obtain the Leaf Age and Plant Centre of Weeds in Complex Field Environments. *Sensors* **2021**, *21*, 3389. [[CrossRef](#)]
43. Nazari Galedar, M.; Jafari, A.; Mohtasebi, S.S.; Tabatabaefar, A.; Sharifi, A.; O'Dogherty, M.J.; Rafiee, S.; Richard, G. Effects of Moisture Content and Level in the Crop on the Engineering Properties of Alfalfa Stems. *Biosyst. Eng.* **2008**, *101*, 199–208. [[CrossRef](#)]
44. Zhang, Y.; Cui, Q.; Guo, Y.; Li, H. Experiment and Analysis of Cutting Mechanical Properties of Millet Stem. *Trans. Chin. Soc. Agric. Mach.* **2019**, *50*, 146–155+162.
45. Qi, L.; Liang, Z.; Ma, X.; Tan, Y.; Jiang, L. Validation and Analysis of Fluid-Structure Interaction between Rotary Harrow Weeding Roll and Paddy Soil. *Nongye Gongcheng Xuebao/Trans. Chin. Soc. Agric. Eng.* **2015**, *31*, 29–37. [[CrossRef](#)]
46. Tang, H.; Xu, C.; Wang, Q.; Zhou, W.; Wang, J.; Xu, Y.; Wang, J. Analysis of the Mechanism and Performance Optimization of Burying Weeding with a Self-Propelled Inter Row Weeder for Paddy Field Environments. *Appl. Sci.* **2021**, *11*, 9798. [[CrossRef](#)]
47. Xu, J.; Sun, S.; He, Z.; Wang, X.; Zeng, Z.; Li, J.; Wu, W. Design and Optimisation of Seed-Metering Plate of Air-Suction Vegetable Seed-Metering Device Based on DEM-CFD. *Biosyst. Eng.* **2023**, *230*, 277–300. [[CrossRef](#)]
48. Smith, R.J.; Fox, W.T. Soil Water and Growth of Rice and Weeds. *Weed Sci.* **1973**, *21*, 61–63. [[CrossRef](#)]
49. Custodio, T.; Houle, D.; Girard, F. Impact of Environmental Conditions on Seed Germination of Glossy Buckthorn (*Frangula Alnus* (Mill)) in Eastern Canada. *Forests* **2023**, *14*, 1999. [[CrossRef](#)]
50. Goksel Pekitkan, F. Mechanical Properties of Okuzgozu (*Vitis vinifera* L. Cv.) Grapevine Canes. *J. King Saud Univ. Sci.* **2024**, *36*, 103034. [[CrossRef](#)]
51. Wu, K.; Song, Y. Research Progress Analysis of Crop Stalk Cutting Theory and Method. *Trans. Chin. Soc. Agric. Mach.* **2022**, *53*, 1–20.
52. Igathinathane, C.; Womac, A.R.; Sokhansanj, S. Corn Stalk Orientation Effect on Mechanical Cutting. *Biosyst. Eng.* **2010**, *107*, 97–106. [[CrossRef](#)]
53. Kumar, A.A.; Tewari, V.K.; Nare, B. Embedded Digital Draft Force and Wheel Slip Indicator for Tillage Research. *Comput. Electron. Agric.* **2016**, *127*, 38–49. [[CrossRef](#)]
54. Wang, Y.; Xi, X.; Chen, M.; Shi, Y.; Zhang, Y.; Zhang, B.; Qu, J.; Zhang, R. Design of and Experiment on Reciprocating Inter-Row Weeding Machine for Strip-Seeded Rice. *Agriculture* **2022**, *12*, 1956. [[CrossRef](#)]

Disclaimer/Publisher's Note: The statements, opinions and data contained in all publications are solely those of the individual author(s) and contributor(s) and not of MDPI and/or the editor(s). MDPI and/or the editor(s) disclaim responsibility for any injury to people or property resulting from any ideas, methods, instructions or products referred to in the content.